



# Intravital longitudinal imaging of hepatic lipid droplet accumulation in a murine model for nonalcoholic fatty liver disease

JIEUN MOON,<sup>1,2</sup> EUNJI KONG,<sup>2,3</sup>  JINGU LEE,<sup>1,2</sup> JINJOO JUNG,<sup>4</sup>  
EUNHA KIM,<sup>5</sup> SEUNG BUM PARK,<sup>4,6</sup> AND PILHAN KIM<sup>1,2,3,\*</sup> 

<sup>1</sup>Graduate School of Nanoscience and Technology, Korea Advanced Institute of Science and Technology (KAIST), 291 Daehak-ro, Yuseong-gu, Daejeon, 34141, South Korea

<sup>2</sup>KI for Health Science and Technology (KIHST), Korea Advanced Institute of Science and Technology, (KAIST), 291 Daehak-ro, Yuseong-gu, Daejeon, 34141, South Korea

<sup>3</sup>Graduate School of Medical Science and Engineering, Korea Advanced Institute of Science and Technology (KAIST), 291 Daehak-ro, Yuseong-gu, Daejeon, 34141, South Korea

<sup>4</sup>Department of Chemistry, Seoul National University, 1 Gwanak-ro, Gwanak-gu, Seoul, 08826, South Korea

<sup>5</sup>Department of Molecular Science and Technology, Ajou University, 206 Worldcup-ro, Yeongtong-gu, Suwon, 16499, South Korea

<sup>6</sup>Department of Biophysics and Chemical Biology, Seoul National University, 1 Gwanak-ro, Gwanak-gu, Seoul, 08826, South Korea

\*[pilhan.kim@kaist.ac.kr](mailto:pilhan.kim@kaist.ac.kr)

**Abstract:** Nonalcoholic fatty liver disease (NAFLD) is a rapidly increasing chronic liver disorder worldwide accompanied by hepatic steatosis, inflammation, fibrosis, and severe liver failure. Unfortunately, an effective treatment strategy for NAFLD has not yet been established, which has been hampered by the limited understanding of the pathophysiological drivers for NAFLD. To examine the unknown cellular and molecular mechanisms in the pathogenesis of NAFLD, there is an increasing need for the direct *in vivo* observation of hepatic microenvironments over extended periods of time. In this work, using a custom-built intravital imaging system and a novel fluorescent lipid droplet labeling dye, Seoul-Fluor 44 (SF44), we established an intravital imaging method to visualize individual lipid droplets and microvasculature simultaneously in the liver of live mice *in vivo*. In addition, in the nonalcoholic steatosis and steatohepatitis mouse model induced by a methionine and choline-deficient diet, we longitudinally visualized and quantitatively analyzed the development of lipid droplets in hepatocytes and sinusoid at a subcellular resolution during the progression of NAFLD up to 21 days *in vivo*.

© 2020 Optical Society of America under the terms of the [OSA Open Access Publishing Agreement](#)

## 1. Introduction

In recent years, there has been a rapidly increasing interest in nonalcoholic fatty liver disease (NAFLD) with a high prevalence in the world. In 2018, the global prevalence of NAFLD is estimated at 25% in adults; the highest rates are presented from South America at 30% and the Middle East at 32%, followed by Asia at 27%, the USA at 24%, and Europe at 24% [1–6]. In the United States, several studies reported that NAFLD is the second leading etiology in 2013 and is expected to become a leading indicator in a population who will require liver transplantation in the next 20 years [7,8]. NAFLD has been attributed to central obesity [9], type 2 diabetes [10,11], and insulin resistance [12], which suggests NAFLD is a hepatic manifestation of metabolic syndrome. The most common form of NAFLD is hepatic steatosis, accumulation of excess fat in liver, which is the first histologic feature of the early stage of NAFLD. Hepatic cellular lipid overload leads to increased oxidative stress and mitochondrial dysfunction, which can induce a severe inflammatory response with upregulation of pro-inflammatory cytokines [13]. Then it

can progress to more serious conditions such as nonalcoholic steatohepatitis (NASH) [14,15], activation of fibrosis [16,17], cirrhosis [18] and ultimately hepatocellular carcinoma [19,20].

After the transition from NASH to fibrosis happens, it is very difficult to recover the liver to a normal condition. Thus, over the last decade, there has been numerous efforts to develop novel therapeutics to intervene in the stage of NASH. However, the underlying cellular and molecular mechanisms in the pathogenesis of NASH have still remained mostly enigmatic due to its highly complex multifactorial dynamics involving multiple hepatic microenvironment components. Currently, an effective treatment strategy of NASH has remained elusive, and there are no pharmacological therapies for NASH [21,22]. Recently, there are increasing evidences claiming that hepatic steatosis is one of the driving forces in the transition to NASH, yet the dynamic development of hepatic LDs during NASH progression has not been well studied. Furthermore, conventional histological evaluation of postmortem liver tissue precludes our ability to dissect the dynamically varying pathological phenotypes in various stages of NAFLD progression. To more efficiently investigate the unknown cellular and molecular mechanisms in the pathogenesis of NAFLD in a complex *in vivo* hepatic microenvironment, a repetitive and longitudinal intravital visualization of the liver during NAFLD progression from the hepatic steatosis stage is a highly desirable approach.

Seoul-Fluor 44 (SF44) is a newly developed fluorescence dye which can selectively label cellular LDs in adipocyte in *in vitro* condition with a very low background within a few minutes [23,24]. However, a direct *in vivo* visualization of LD accumulation in a NAFLD mouse model using SF44 has not been achieved yet.

In this work, using a custom-built intravital confocal microscopy system [25–30], we successfully visualized individual LDs in hepatocytes in the liver of live mice *in vivo* with intravenous injection of SF44. In addition, in the nonalcoholic hepatic steatosis and NASH mouse model induced by a methionine and choline-deficient (MCD) diet [31,32], we longitudinally visualized and quantitatively analyzed the gradual accumulation of hepatic LDs and their changes with the liver sinusoid simultaneously during the progression of hepatic steatosis in a cellular resolution up to 21 days *in vivo*.

## 2. Methods

### 2.1. Animal

All animal experiments were performed in accordance with the health guidelines for the use of experimental animals and were approved by the Institutional Animal Care and Use Committee (IACUC) of Korea Advanced Institute of Science and Technology (protocol no. KA-2018-78). All mice were individually housed in ventilated and temperature & humidity-controlled cages (22.5 °C, 52.5%) under 12:12 hours light:dark cycle and provided with standard diet and water *ad libitum*. Male C57BL/6 mice purchased from OrientBio (Suwon, Rep. of Korea) were used for all experiments. To induce nonalcoholic steatosis and steatohepatitis, mice were fed with a methionine and choline-deficient (MCD) diet (Envigo, USA). To observe temporal LD dynamics during the transition from normal liver to nonalcoholic hepatic steatosis, 4 groups of mice fed MCD with different period; 2, 7, 14, 21 days. The mice as control were fed with normal diet for the same period. 3 mice were used for each experiment group. All mice were 10 weeks of age at the commencement of each diet.

### 2.2. Intravital imaging system

To visualize the *in vivo* hepatic microenvironment in MCD diet-induced NAFLD mouse model, a custom-built video-rate laser-scanning confocal microscopy system previously demonstrated was used [25–30]. For SF44 and anti-CD31 antibody conjugated with Alexa Fluor 647 fluorescence imaging, 488nm laser (MLD488, Cobolt), and 640nm laser (MLD640, Cobolt) were used as

excitation laser sources with optical power of 284  $\mu\text{W}$ , and 196  $\mu\text{W}$  measured at sample plane, respectively. Video rate Raster-pattern laser-scanning at 30 Hz was achieved by using a 36-facet polygonal mirror rotating at 480 revolutions per second (MC-5, aluminum coated, Lincoln Laser) for fast-axis scanning and a galvanomirror scanner operating at 30 Hz (6230H, Cambridge Technology) for slow-axis scanning. The scanning laser beam was delivered to the anesthetized mouse on XYZ translation stage (3DMS, Sutter Instrument) through commercial objective lenses PlanApo $\lambda$ 20X (Nikon, 20 $\times$ , 0.75NA) and LUMFLN60X (Olympus, 60 $\times$ , 1.1NA) providing the field of views (FOV) of 568  $\times$  568  $\mu\text{m}$ , 164  $\times$  164  $\mu\text{m}$ , respectively. Multi-color fluorescence signals excited by the lasers were simultaneously detected by three photomultiplier tubes (PMT; R9110, Hamamatsu) equipped with bandpass filters (FF02-525/50, FF01-600/37, FF01-697/58, Semrock) respectively. Electronic signals from the PMTs were acquired by a 4-channel frame grabber (Solios, Matrox). Video-rate images acquired at frame rate of 30 Hz with frames size of 512  $\times$  512 pixels were displayed and stored in real-time by a custom-written software based on Matrox Imaging Library (MIL9, Matrox).

### 2.3. Intravital liver imaging

#### ■ Intravital imaging preparation

Liver sinusoid endothelial cells were labelled *in vivo* by intravenous injection of 25  $\mu\text{g}$  of anti-CD31 monoclonal antibody (553370, BD Bioscience) conjugated with Alexa Fluor 647 (A20186, Invitrogen) at 2 hours before the intravital imaging. Hepatic LDs were labeled by intravenous injection of 120  $\mu\text{l}$  of 1.67 mM SF44 (SPARK Biopharma) at 30 minutes before the intravital imaging. The absorption / emission peak wavelength are 445 nm / 611 nm for SF44 and 651 nm / 667 nm for Alexa Fluor 647, respectively. And the fluorescence signal of SF44 and Alexa Fluor 647 were detected through optical bandpass filters with wavelength band of 581.5 nm – 618.5 nm and 668 nm – 726 nm, respectively. Mice were anesthetized with intraperitoneal injection of the mixture of Zoletil (20 mg/kg) and Xylazine (11 mg/kg). After the anesthetization, abdominal hair was removed by using hair clipper and hair removal cream. Small incision with size of 10 mm was made on skin and peritoneum, then the left lobe of liver was exteriorized and positioned on a wet gauze to reduce motion artifact by separating other tissues near left lobe. The cover glass attached with a customized heater and commercial thermometer was placed on the exteriorized left lobe of liver, which maintain the temperature of local liver tissue constant at 36  $^{\circ}\text{C}$  during the intravital imaging. In addition, using a commercial homeothermic heating pad (RightTemp Jr., Kent Scientific) for small animal, the body temperature of the anesthetized mouse was also maintained at 36  $^{\circ}\text{C}$  during the intravital imaging. To prevent the surface of the exteriorized liver tissue from being dry, warmed saline was continuously supplied during the imaging.

#### ■ Intravital time-lapse imaging of temporal decay of SF44 fluorescent intensity

To investigate the temporal decay of fluorescent intensity of SF44-labeled hepatic LDs after the intravenous injection of SF44, time-lapse imaging was performed at the same location for 6 hours with different time intervals (10 minutes until 90 minutes, 30 minutes from 90 to 180 minutes, 60 minutes from 180 to 360 minutes). During *in vivo* imaging for 6 hours, the level of anesthetization was continuously monitored by pinching toe. Whenever the response was observed, anesthetization was maintained by intramuscular injection with half dose zoletil / xylazine mixture. Images were acquired by using a 20 $\times$  objective lens (PlanApo $\lambda$ 20X, 0.75NA, Nikon) providing FOV of 568  $\times$  568  $\mu\text{m}$  with number of pixels of 512  $\times$  512 pixels and pixel size of 1.11  $\mu\text{m}$ . To enhance the signal-to-noise ratio, each image was obtained by averaging 90 frames acquired at video-rate of 30 fps for 3 seconds.

### ■ *Intravital z-stack imaging of LD accumulation in hepatocyte*

Z-stack images were acquired from the surface of the liver tissue to the deeper sinusoid bed with hepatocytes (total 40  $\mu\text{m}$  in depth) by sequential imaging along the z-axis with 2  $\mu\text{m}$  intervals. Images were acquired by using a 60 $\times$  objective lens (LUMFLN60X, 1.1NA, Olympus) providing FOV of 164  $\times$  164  $\mu\text{m}$  with number of pixels of 512  $\times$  512 pixels and pixel size of 0.32  $\mu\text{m}$ . To enhance the signal-to-noise ratio, each image was obtained by averaging 90 frames in all experiments. For quantitative analysis, we obtained z-stack images at 10 randomly selected spots in the liver of each mouse.

#### 2.4. *Imaging analysis and statistical analysis*

Volume of hepatic LD was quantified from the 3D-rendered image reconstructed from z-stack images of 20- $\mu\text{m}$  thickness covering sinusoidal networks and hepatocyte. To quantify volume of hepatic LD, the sequential z-stack images were converted to 3D-rendered image with commercial image analysis software, IMARIS (Bitplane). All LDs in the imaging volume were automatically identified and quantified using the Surface function of IMARIS. To distinguish each individual spherical shaped LDs from contiguous neighbor LDs, we set the parameters in the Surface function, the Diameter of Largest Sphere and the Surface Area Detailed Level to 5  $\mu\text{m}$  and 0.5  $\mu\text{m}$ , respectively. Then, the automatically measured volume values of all hepatic LD in the imaging volume were exported for quantification analysis. LD volumetric ratio was calculated with by dividing the total volume of hepatic LDs with total imaging volume. To quantify the number and diameter of LDs, all images were converted to binary images with threshold set as 196, which is 77% of the maximum value in 8-bit image, 255. Then the number and diameter of LDs were measured using Scale and Measure function of Image J (NIH). With values of volume, diameter, and number of LD, fractional ratio of groups of hepatic LDs with different diameters. Statistical analysis was performed by using Origin (OriginLab). Data are presented as mean  $\pm$  SD. 3 mice were analyzed for each experimental group. Statistical differences were determined by two-tailed unpaired Student's t-test. Statistical significance was set at p-value less than 0.05.

### 3. Results

#### 3.1. *Intravital imaging of hepatic LDs in a MCD-diet induced NASH mouse model*

To perform intravital imaging of hepatic LD accumulation in MCD-diet induced NASH mouse model, the left lobe of liver was exposed by laparotomy and carefully positioned on wet gauze to minimize motion by separating the lobe from neighboring internal organs such as intestine and a cover glass with silicone rubber heater was placed on the exteriorized lobe as shown in Fig. 1(a,b). The liver of mice fed with the MCD diet suffers metabolic imbalances of fat with an excessive influx of free fatty acids (FFAs). In the liver, FFAs are esterified to triglyceride (TG), which accumulates in the cytoplasm of hepatocytes in the form of lipid droplets (LDs). As shown in Fig. 2(a,b), with intravenously injected SF44, we successfully visualized individual LDs of various sizes in the range of 3 to 10  $\mu\text{m}$  accumulated in the hepatocytes in the liver of live anesthetized mice fed the MCD diet for 28 days *in vivo*. Of note, the liver sinusoid endothelial cells expressing CD31 were simultaneously visualized with *in vivo* fluorescence labeling by intravenous injection of anti-CD31 antibody conjugated with a far-red fluorophore, Alexa Fluor 647. In the liver of mice fed a normal diet for the same period, in contrast, only small scattered LDs with a diameter of about 1  $\mu\text{m}$  were observed (Fig. 2(a)–2(b)). In addition, we confirmed the induction of hepatic steatosis in the MCD diet mouse liver by conventional histopathological analysis with hematoxylin and eosin (H&E) staining, which showed the ballooning of enlarged hepatocytes with a rarefied cytoplasm occupied by lipids and displaced nuclei to the periphery, which are the hallmark of NASH [33,34] (Fig. 2(c)).

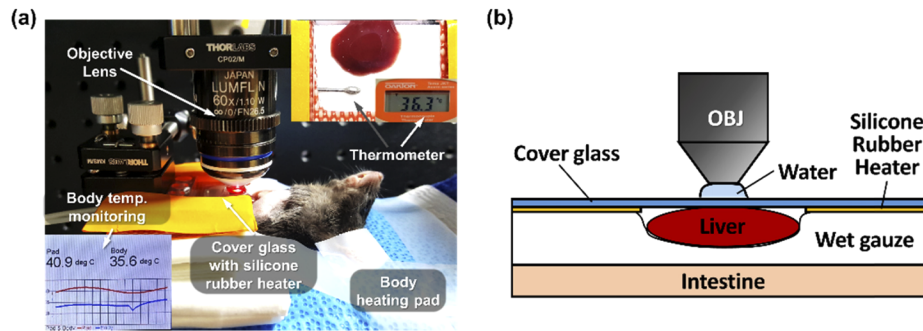
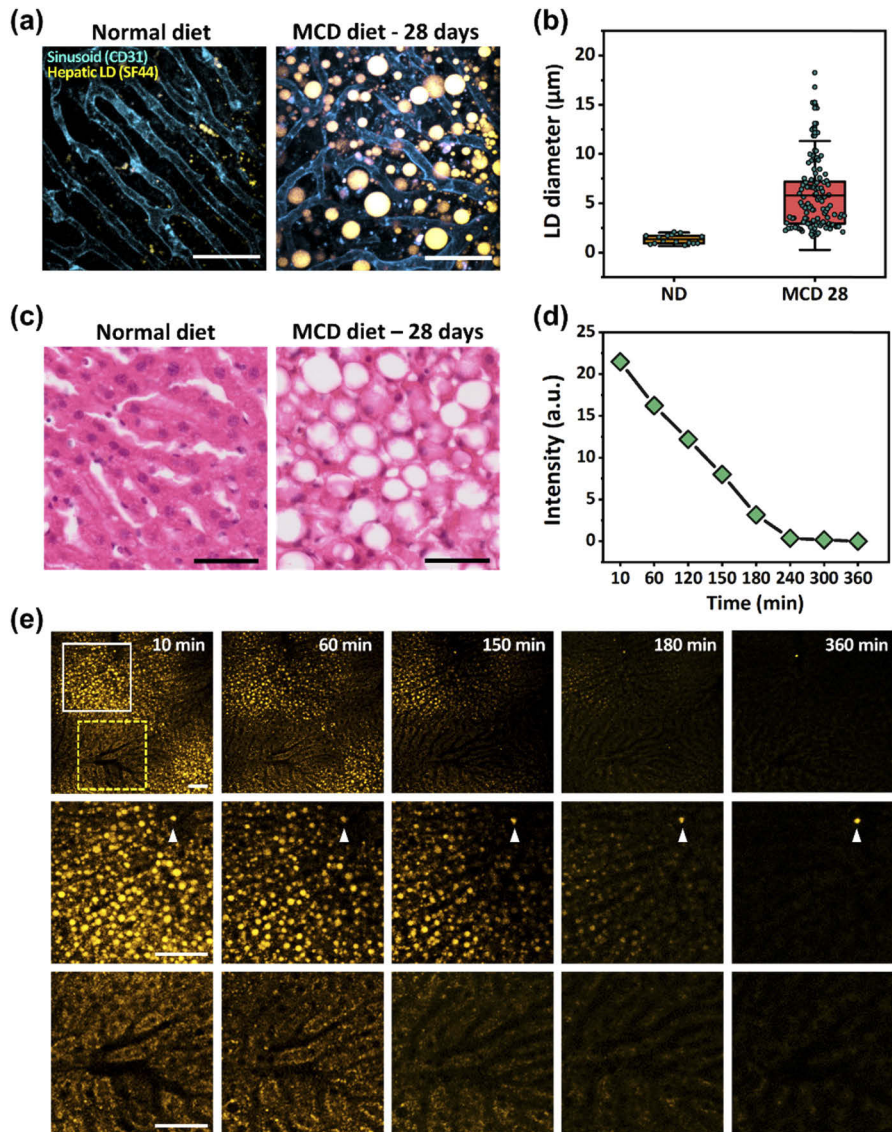


**Fig. 1. Intravital liver imaging setup.** (a) Photograph of intravital liver imaging setup. Heating pad for body temperature maintenance of the anesthetized mouse and silicone rubber heater for temperature maintenance of exposed liver were used. (b) Schematic of exposed liver positioning on wet gauze to minimize motion and humidity maintenance.

Next, we monitored the clearance of SF44 from the liver of the mouse fed the MCD diet for 28 days after the intravenous injection of SF44 for 6 hours by time-lapse intravital imaging (Fig. 2(d)–2(e)). Figure 2(d) shows the temporal decay of the fluorescence intensity of SF44-labeled LDs quantified from wide-area images in Fig. 2(e), which decreased for 4 hours to almost an undetectable level. In comparison with the initial value at 10 minutes, the fluorescence intensity of SF44 was decreased to 75.6% at 60 minutes, 56.8% at 120 minutes, 14.8% at 180 minutes and finally to 1.7% at 240 minutes, suggesting almost a complete clearance of SF44 from the liver within 4 hours after the intravenous injection. Figure 2(e) shows sequential images obtained from the liver from 10 minutes after the intravenous injection of SF44 until 6 hours. All images were obtained with same excitation laser power and detector sensitivity. Interestingly, SF44 could rapidly and uniformly label hepatic LDs with high contrast *in vivo* in 10 minutes after the intravenous injection shown in the magnified image marked by a white solid-line box in Fig. 2(e). In the hepatocytes with much less accumulated LDs presumably in the periportal area [35] known to have reduced lipogenesis and triglyceride accumulation [36,37], SF44 was uniformly distributed in the cytoplasm and did not penetrate into nucleus shown in the magnified image marked by a yellow dotted-line box in Fig. 2(e). Then, in both areas, SF44 was gradually cleared over time without leaving any non-specific labeling of cellular or extracellular components. Of note, the bright dot remaining at 6 hours marked by the arrow head in Fig. 2(e) was autofluorescence, which shows little change in the fluorescence intensity; thus, it is clearly differentiated with SF44 fluorescence signal.

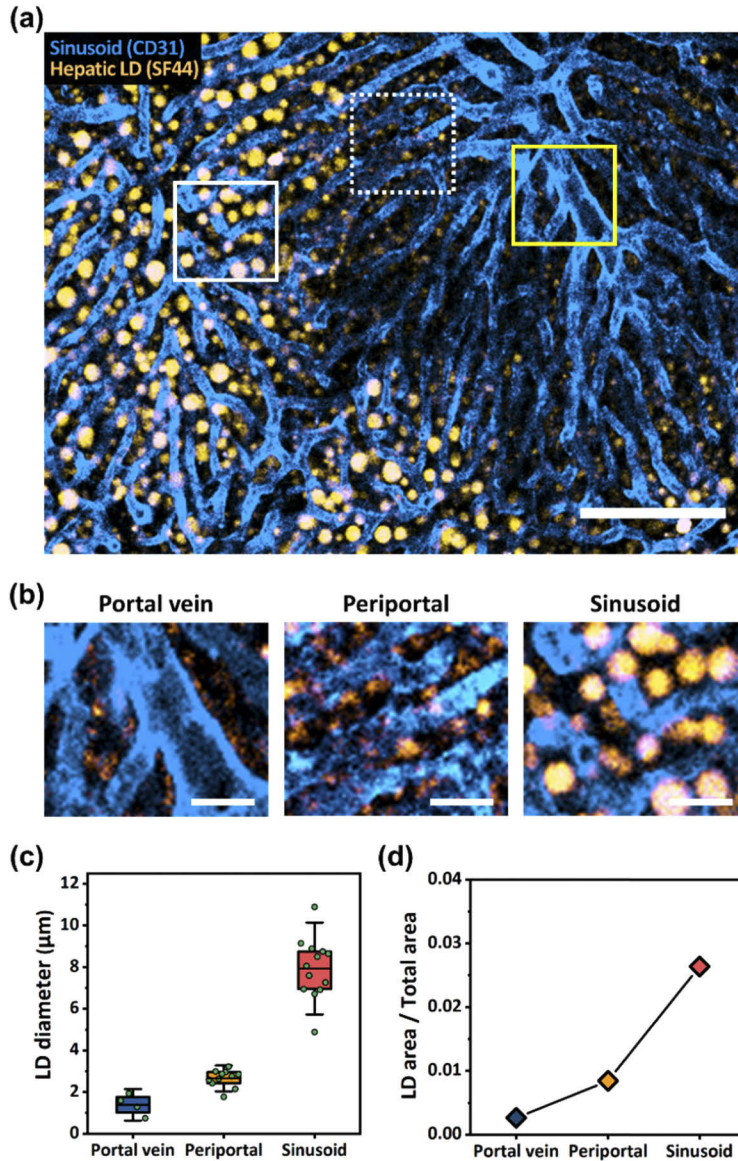
### 3.2. Intravital imaging of a wide-area distribution of hepatic LDs in the MCD-diet induced NASH mouse model

Figure 3(a) shows a wide-area image obtained *in vivo* from the liver of mice fed the MCD diet for 14 days. LDs and endothelial cells were simultaneously visualized *in vivo* by intravenously injected SF44 and ant-CD31 antibody-fluorophore conjugates, respectively. Similar to the observation in Fig. 2(e), the size and degree of LD accumulation in hepatocytes are non-uniform depending on the areas discriminated by distinct vascular morphologies, portal vein and sinusoid. The portal vein with a larger diameter of 20–35  $\mu\text{m}$  and the connected capillary, the liver sinusoids with a typical diameter of 7–14  $\mu\text{m}$ , were clearly identifiable [38]. Figure 3(b) shows magnified images at three representative areas of the liver with different LDs accumulation: the portal vein area, periportal area and sinusoid area marked by a yellow solid-line square, white dotted-line square and white solid-line square in Fig. 3(a), respectively. As clearly seen in Fig. 3(b), larger LDs only accumulated in the hepatocytes that were farther away from the portal vein. In the



**Fig. 2.** Intravital imaging of SF44-labeled hepatic LDs in MCD-diet induced NASH mouse model. (a) *In vivo* images of hepatic LDs (yellow, SF44) and sinusoid (cyan, CD31) in the liver of mice fed the normal diet or MCD diet for 28 days. Scale bars, 50  $\mu\text{m}$ . (b) Diameter of LD in ND or MCD for 28 days shown on (a). (c) Histopathological hematoxylin and eosin (H&E) staining images of the livers of mice fed the normal diet or MCD diet for 28 days. Scale bars, 50  $\mu\text{m}$ . (d) Graph of temporal changes in the fluorescence intensity of SF44 in the liver of mice fed the MCD diet for 28 days after the intravenous injection of SF44. (e) Wide-area (top row) and magnified (solid-, yellow dotted-line box, respectively) sequential images of the hepatic LDs (yellow) after intravenous injection of SF44 obtained with same excitation laser power and detector sensitivity. Scale bars, 50  $\mu\text{m}$ .

hepatocytes adjacent to the portal vein, the mean LD diameter was only 1.39  $\mu\text{m}$ , similar to the value observed in the hepatocytes of the liver from the normal-diet mouse. In the hepatocytes in the periportal area, the mean LD diameter was increased to 2.66  $\mu\text{m}$ . In the hepatocytes between the sinusoids, the mean LD diameter was greatly increased to 7.94  $\mu\text{m}$  (Fig. 3(c)). The LD area of total area was increased due to large LD accumulation in the sinusoid region compared with portal vein region (Fig. 3(d)).



**Fig. 3. Spatial distribution of hepatic lipid droplet in MCD diet-induced NASH mouse model.** (a) Wide-area *in vivo* image showing spatially distributed different-sized hepatic lipid droplets in the liver of mouse fed MCD diet for 14 days. Scale bar, 100  $\mu\text{m}$ . (b) Magnified images of (a) marked by yellow solid-lined box (portal vein), white dotted-lined box (periportal) and white solid-lined box (sinusoid), respectively. Scale bars, 20  $\mu\text{m}$ . (c,d) LD diameter and LD area, respectively at portal vein, periportal, and sinusoid shown on (b).

### 3.3. Longitudinal intravital imaging of hepatic LD development in the MCD-diet induced NASH mouse model

To observe the hepatic LD development during the progression of NAFLD, we longitudinally imaged the liver of mice fed the MCD diet up to 21 days *in vivo* by acquiring z-stack images with a custom-built intravital confocal microscopy system. Figure 4(a) shows the representative maximum intensity projection z-stack image data obtained after 2, 7, 14 and 21 days of the MCD diet. With the continued feeding of the MCD diet, the size of the individual hepatic LDs in the hepatocytes gradually increased until 21 days. After only 2 days of the MCD diet, numerous microvesicular LDs were observed (Fig. 4(a)–4(b)). More than half of the observed hepatic LDs were less than 3  $\mu\text{m}$  in diameter. After 7 days of the MCD diet, the number of hepatic LDs was decreased while the size of the individual LDs was increased; the ratio of macrovesicular-shaped hepatic LDs became larger than the microvesicular-shaped hepatic LDs. As the period of the MCD diet increased, the size of the individual hepatic LDs became larger. After 21 days of the MCD diet, many very large LDs with a diameter larger than 10  $\mu\text{m}$  were observed. In contrast, in the liver of the mouse fed the normal standard diet, only a few small hepatic LDs mostly smaller than 1  $\mu\text{m}$  in diameter were observed.

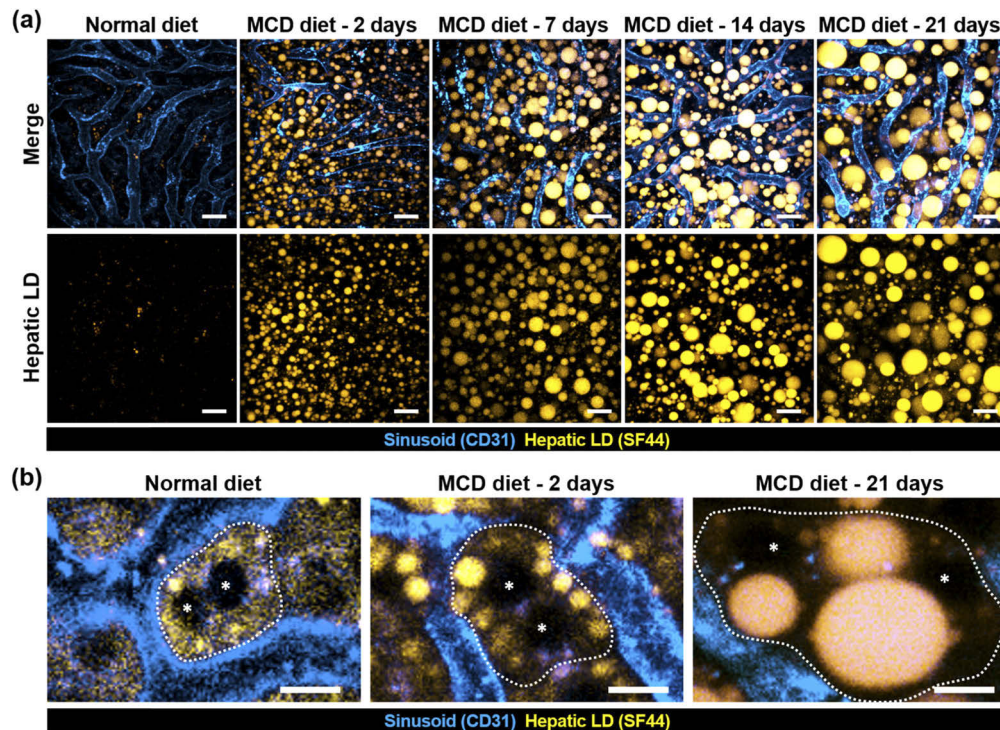


**Fig. 4.** Longitudinal intravital imaging of hepatic lipid droplet accumulation in MCD-diet induced NASH mouse model. (a) Representative maximum intensity projection (MIP) images of hepatic LD (yellow, SF44) and sinusoid (cyan, CD31) in the liver of mice fed normal diet or MCD diet. Scale bars, 20  $\mu\text{m}$ . (b) Representative magnified *in vivo* images of single hepatocyte showing the position of nuclei (asterisks) and boundary (dotted line). Scale bars, 10  $\mu\text{m}$ .

In addition, we could clearly identify the subcellular-level change of the nucleus position in a single hepatocyte due to the formation of a large macrovesicular LD *in vivo*. A hepatocyte is a polynuclear parenchymal cell with multiple nuclei, which are normally located at the center of

the cell body shown in the image obtained from the mouse fed the normal diet in Fig. 4(b). Of note, the boundary of the hepatocytes was marked by dotted lines, and the nuclei were marked by asterisks. At the initial stage of NAFLD with 2 days of the MCD diet, the position of two nuclei in a single hepatocyte nucleus was remained at the center with multiple microvesicular LDs in the cytoplasm. In contrast, after 21 days of the MCD diet, very large macrovesicular LDs were formed in the cytoplasm and displaced the position of the nuclei to the periphery of the hepatocyte, which is a well-known subcellular-level feature of NASH [33,34].

To perform the quantitative analysis of the dynamic changes in hepatic LD development during the progression of NAFLD, volumetric 3D rendered images were generated using *in vivo* z-stack images longitudinally acquired at 2, 7, 14 and 21 days of the MCD diet. Of note, in each group, z-stack images were obtained at 10 randomly selected locations in the exposed left lobe of the liver to minimize the variation between the imaged areas and to avoid potential bias although the

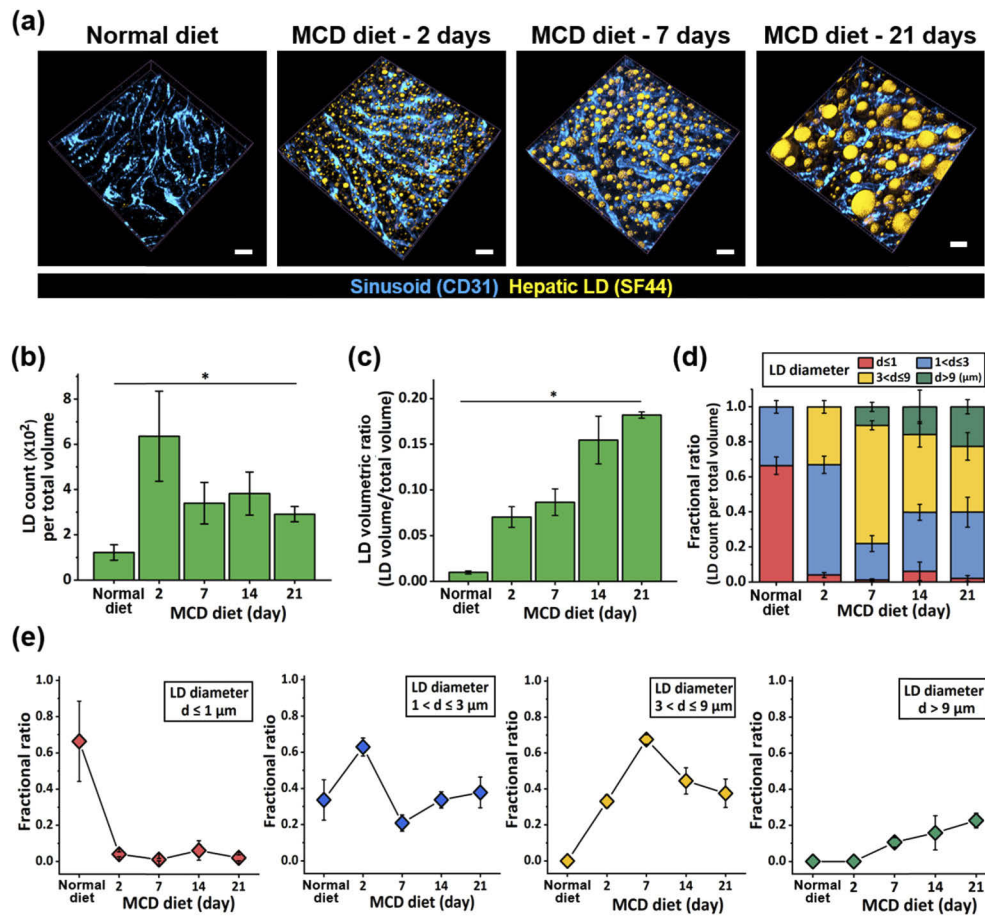


**Fig. 5. Quantitative analysis of longitudinal accumulation of hepatic lipid droplet in MCD-diet induced NASH mouse model.** (a) Representative 3D rendered image of hepatic lipid droplets (green, SF44) and sinusoid (red, CD31) in the liver of mice fed normal diet or MCD diet. Scale bars, 20  $\mu\text{m}$ . (b) Number of hepatic lipid droplets. (c) Volumetric ratio of hepatic lipid droplets. (d) Fractional ratio of groups of hepatic lipid droplets with different diameters;  $d < 1 \mu\text{m}$ ,  $1 < d \leq 3 \mu\text{m}$ ,  $3 < d \leq 9 \mu\text{m}$ ,  $d > 9 \mu\text{m}$ . (e) Fractional ratio of hepatic lipid droplet in each group. (d–e) Data are presented as mean  $\pm$  standard error of mean. 3 mice were analyzed for each group.

liver is known to be relatively homogeneous. Figure 5(a) shows the representative 3D rendered images showing the vasculature and hepatic LDs accumulated in the liver of the mice fed the MCD diet. Utilizing the 3D rendered images, we could quantify the longitudinal changes in the number of hepatic LDs and the ratio of the volume occupied by LDs to the total imaging volume as shown in Fig. 5(b) and 5(c), respectively. At 2 days of the MCD diet, the number of hepatic LD (636) was greatly increased about 5 times in comparison to the number observed in the liver fed the normal diet (129), reflecting the formation of numerous microvesicular LDs by impaired hepatic lipid metabolism acutely induced by the MCD diet. Similarly, the volumetric ratio of the hepatic LDs was greatly increased to 7.03% more than 7 times in comparison to that of the normal diet, 0.98%. At 7 days of the MCD diet, the number of hepatic LDs was significantly decreased to 340 due to the fusion of the microvesicular hepatic LDs closely located to each other, which then remained at a similar value until 21 days of the MCD diet shown in Fig. 5(b). In contrast, the volumetric ratio of the hepatic LDs continuously increased with the MCD-diet shown in Fig. 5(c). After 21 days of the MCD-diet, the hepatic LDs accounted for more than 18% of the total imaging volume.

As previously described in Fig. 4(a), as the period of the MCD diet increased, the size of the individual hepatic LDs became larger. To quantify this development of the group of hepatic LDs over time, we divided the observed LDs into 4 groups by diameter:  $d \leq 1 \mu\text{m}$ ,  $1 < d \leq 3 \mu\text{m}$ ,  $3 < d \leq 9 \mu\text{m}$ , and  $9 \mu\text{m} < d$ . Figure 5(d–e) shows the changes of the fractional ratio of each group occupied in the total volume of the LDs. In the healthy liver with the normal diet, all of the observed hepatic LDs are smaller than  $3 \mu\text{m}$  in diameter and more than 65% of them are smaller than  $1 \mu\text{m}$ . Surprisingly, only after 2 days of the MCD diet, the portion of newly appeared hepatic LDs bigger than  $3 \mu\text{m}$  in diameter reached more than 30% and the portion of LDs smaller than  $1 \mu\text{m}$  was greatly decreased to below 4% in striking comparison to 66% in the normal liver shown in Fig. 5(d). After 7 days of the MCD diet, almost 80% of the hepatic LDs became bigger than  $3 \mu\text{m}$  in diameter. Very large LDs bigger than  $9 \mu\text{m}$  in diameter newly appeared, which occupied more than 10% of all the observed LDs. With the sustained MCD diet, the portion of very large hepatic LDs continuously increased and accounted for more than 22% of all the observed LDs at 21 days. In addition, we quantified the changes of the sinusoid diameter using the longitudinally acquired images, which showed no statistical differences until 21 days of MCD diet. Figure 6(a) shows the representative images of liver sinusoid in the mouse fed the normal diet and the MCD diet for 21 days. In the liver of the mouse fed the MCD diet for 21 days, there existed a few sinusoid branches with a decreased diameter, and the average diameter of the sinusoid ( $5.70 \mu\text{m}$ ) was narrower than that of the normal liver ( $7.48 \mu\text{m}$ ) but with no statistical significance (Fig. 6(b)).

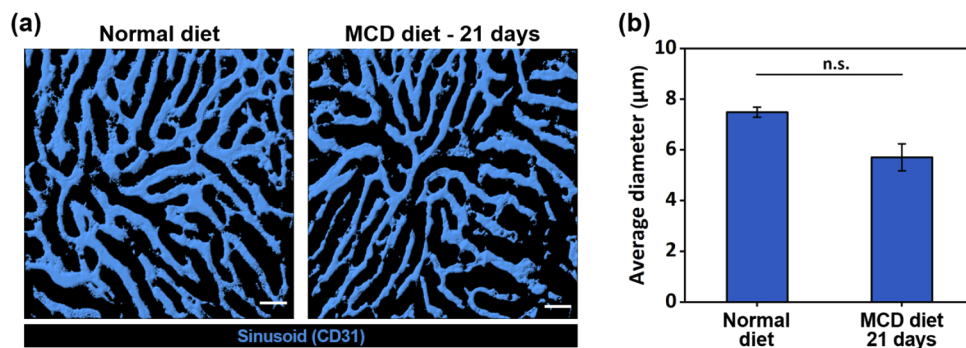


**Fig. 6. Quantitative analysis of sinusoid in MCD-diet induced NASH mouse model.** (a) Representative image of sinusoid area in the liver of mice fed normal diet or MCD diet. Scale bars,  $50 \mu\text{m}$ . (b) Average diameter of sinusoid in normal diet or MCD diet.

#### 4. Discussion

In this work, we successfully visualized hepatic LDs in the liver of live mice *in vivo* at the subcellular-level using SF44 [23,24] and a custom-built video-rate laser-scanning confocal intravital microscopy system [25–30] (Fig. 2). To demonstrate the capability of SF44 for the *in vivo* visualization of hepatic LDs, we utilized a NAFLD/NASH mouse model induced by a methionine and choline-deficient (MCD) diet [31,32], which has been one of the most extensively used models for NAFLD/NASH research [39]. Methionine and choline have a pivotal role in mitochondrial  $\beta$ -oxidation, secretion of very low density lipoprotein (VLDL) and many essential cellular processes involved in lipid metabolism in the hepatocytes of the liver. Feeding a MCD diet induces NASH in a mouse, which is characterized by hepatic steatosis, mitochondrial dysfunction, increased oxidative stress, hepatocellular injury, inflammation and fibrosis [40]. Indeed, in the liver of the MCD diet-induced NASH mouse model, we successfully visualized the subcellular-level hallmarks of NASH *in vivo* using SF44 such as the accumulation of macrovesicular LDs in hepatocytes, ballooning of enlarged hepatocytes, rarefied cytoplasm and displacement of nuclei to the periphery of hepatocytes, and those have been mostly observed by the conventional histopathological analysis of *ex vivo* liver tissues.

More significantly, as shown in Fig. 2(e), the intravenously injected SF44 was rapidly accumulated in the liver and took up by hepatocytes and then specifically labeled LDs with high contrast and sensitivity within 10 minutes. Furthermore, after the rapid labeling, the SF44 were almost completely cleared out from the hepatocytes in 4 hours presumably through the bile canaliculi, the narrow tube between hepatocytes and the common bile duct, without any remaining non-specific labeling of cellular or extracellular components. This highly preferable kinetics of SF44 could enable us to perform repeated injections of SF44 over time and the longitudinal *in vivo* observation of hepatic LD development with the progression of NAFLD induced by the MCD diet. It also strongly suggests potentially a very low liver toxicity.

In addition, in Fig. 3, we identified the distinct spatial distribution of different sized hepatic LDs *in vivo* according to the location in the liver of the mouse fed the MCD-diet for 14 days. Previous studies have reported that the liver has a distinct microscopic-scale anatomical structure composed of numerous hexagonal-shaped hepatic lobules. The lobule is the functional unit of the liver, which is consisted of portal triad, sinusoids arranged with hepatocytes, and central veins. Along the lobule, in addition, hepatic lobule can be represented in terms of metabolic zones. There exist three distinct zones; periportal (zone 1), mid-zonal (zone 2) and pericentral (zone 3) [48]. In the liver, hepatic blood flows from the portal venules and hepatic arterioles in the portal triad (zone 1) to the sinusoids (zone 2) and finally to the central vein (zone 3). Along with this blood supply pattern through hepatic zonation, there are increasing reports that hepatocytes in each zone has specialized in different metabolic pathways, supporting the concept of metabolic zonation [35,37,48]. The hepatocytes in the periportal region with the portal vein (zone 1) are more engaged in gluconeogenesis and have higher rates of oxidation of free fatty acids. The hepatocytes in the perivenous region with the central vein (zone 3) are more preferentially engaged in glycolysis and lipogenesis. Therefore, it has been suggested that the hepatocytes in the periportal region (zone 1) are less likely exposed to fatty acid accumulation and the hepatic LD accumulation mostly derived by an increased triglyceride pool would occur probably more preferentially in perivenous hepatocytes (zone 3) [36,37]. As clearly seen in Fig. 3(b), larger LDs accumulated only in the hepatocytes that were farther away from the portal vein. Although we did not further analyze specific molecules related in hepatic lipid metabolism according to the distinct zones, on the basis of the previous reports, our observation supports that hepatocytes in the periportal region (zone 1) has a tendency to accumulate smaller-sized LDs, and large LDs are more preferentially accumulated in the sinusoid (zone 2) and the pericentral region (zone 3).

Notably, the longitudinal intravital z-stack imaging revealed dynamic behaviors in the development of subcellular hepatic LDs in hepatocytes with NAFLD progression. Quantitative analysis using 3D rendered images enabled a detailed investigation of cellular- and subcellular-level changes in hepatic LDs such as the rapid formation of microvesicular LDs, their subsequent fusion, formation of macrovesicular LDs, and compositional changes with various sized LDs with the pathogenesis of NAFLD. The newly established method for direct *in vivo* observation of hepatic LDs can be highly useful for future investigation of unknown mechanism in the pathogenesis of NAFLD in the stage of hepatic steatosis and related inflammation or for the *in vivo* evaluation of new therapeutics to reverse NAFLD progression by manipulating the pathological hepatic microenvironment. Although extensive validation would be required for human use, the demonstrated approach of a highly sensitive *in vivo* visualization of hepatic LDs using a fluorescent agent could be developed as a novel diagnostic tools by being incorporated with more clinically viable optical imaging modality such as photoacoustic imaging [41,42] potentially with deep-learning based computer-aided decision system [43]. Meanwhile, several studies have reported that gender difference in incidence of NAFLD evidently exist [44–47], which can be attributed to sexual disparities of fat composition, lifestyle, and sex hormone metabolism. However, in animal model, the correlation between gender and prevalence of NAFLD is not fully defined and longitudinal visualization of hepatic microenvironment would be a useful technique to efficiently investigate the underlying mechanism of gender-based prevalence of NAFLD.

Research to elucidate an unknown pathological driver in NAFLD has been mostly drawn to investigate molecular or signaling pathways. However, analysis of spatiotemporal alterations of hepatic microenvironment at structural levels during NAFLD progression is also insightful research direction because structural change of tissue is associated with dysfunction. Conventional histological observation of postmortem liver tissue has difficulty in dissecting the dynamically varying pathological features in various stages of NAFLD progression. Our intravital visualization approach has an advantage over conventional histology in that we can successfully observe dynamic and temporal development of hepatic LDs in different stages of NAFLD progression. Furthermore, we observed sub-cellular level changes that individual lipid droplet drove morphological change of a hepatocyte. This high resolution temporally resolved quantitative analysis of hepatic LD deposition is capable of revealing unknown morphological features in NAFLD progression. In this work, we only included one-time intravital imaging result obtained from each individual mouse fed with MCD diet for different period of time to observe temporal evolution of LD accumulation without potential impacts of surgical procedure on LD development afterward the intravital imaging. Although data is not shown, we recently succeeded in repeated longitudinal intravital imaging of hepatic LDs in the liver of the same mice 4 times over 4 weeks with repeated intravenous injection of SF44. Whenever intravital liver imaging of the same mice was completed, anti-adhesive agent was applied to prevent excessive adhesion between liver and incised peritoneum, and then incised skin and peritoneum was carefully sutured. Yet, the repeated intravital imaging involving surgical procedure to expose internal organ such as liver has several limitations such as limited number of repetitive imaging depending on the invasiveness of surgical procedure and difficulty in observation of exactly same microscopic location in each repeated imaging session. Currently, several imaging window chamber techniques have been developed to allow repeated imaging of same organ and tissue without the need of repeated surgical exposure [49–52]. Thus, to image the same site over multiple days and weeks, we can adopt previously reported abdominal window imaging technique or develop a novel liver imaging window more optimized for longitudinal observation of hepatic microenvironment.

## 5. Conclusion

In this work, we achieved direct *in vivo* visualization of hepatic LDs in the liver of live mice using a newly developed fluorophore SF44 to label cellular LDs and a custom-built video-rate laser-scanning confocal intravital microscopy system. In the MCD diet-induced NASH mouse model,

we successfully visualized subcellular-level features including accumulation of macrovesicular LDs, hepatocytes ballooning and displacement of nuclei to the periphery. Furthermore, with a longitudinal intravital imaging of a liver of mice fed an MCD diet up to 21 days, we could quantitatively analyze detailed cellular- and subcellular-level development of LDs in hepatocytes such as the formation of micro- and macro-vesicular LDs and the compositional changes with various sized hepatic LDs with the progression from initial hepatic steatosis to NASH. Direct *in vivo* observation of hepatic LDs demonstrated in this work can be a highly useful method for future investigation to explore unknown cellular and molecular mechanism in the pathogenesis of NAFLD or for *in vivo* assessment of novel therapeutics to reverse NAFLD progression alleviating the accumulation of lipids.

## Funding

National Research Foundation of Korea (2014R1A3A2030423, 2016M3C7A1913844, 2017R1E1A1A01074190, 2020R1A2C3005694).

## Acknowledgements

The authors would like to thank Kibaek Choe, Yoonha Hwang for their technical assistances.

## Disclosures

The authors declare that there are no conflicts of interest related to this article.

## References

1. T. Hardy, F. Oakley, Q. M. Anstee, and C. P. Day, "Nonalcoholic Fatty Liver Disease: Pathogenesis and Disease Spectrum," *Annu. Rev. Pathol.: Mech. Dis.* **11**(1), 451–496 (2016).
2. S. L. Friedman, B. A. Neuschwander-Tetri, M. Rinella, and A. J. Sanyal, "Mechanisms of NAFLD development and therapeutic strategies," *Nat. Med.* **24**(7), 908–922 (2018).
3. Z. M. Younossi, "Non-alcoholic fatty liver disease – A global public health perspective," *J. Hepatol.* **70**(3), 531–544 (2019).
4. Z. M. Younossi, A. B. Koenig, D. Abdelatif, Y. Fazel, L. Henry, and M. Wymer, "Global epidemiology of nonalcoholic fatty liver disease—Meta-analytic assessment of prevalence, incidence, and outcomes," *Hepatology* **64**(1), 73–84 (2016).
5. Z. Younossi, F. Tacke, M. Arrese, B. Chander Sharma, I. Mostafa, E. Bugianesi, V. Wai-Sun Wong, Y. Yilmaz, J. George, J. Fan, and M. B. Vos, "Global Perspectives on Nonalcoholic Fatty Liver Disease and Nonalcoholic Steatohepatitis," *Hepatology* **69**(6), 2672–2682 (2019).
6. Z. Younossi, Q. M. Anstee, M. Marietti, T. Hardy, L. Henry, M. Eslam, J. George, and E. Bugianesi, "Global burden of NAFLD and NASH: Trends, predictions, risk factors and prevention," *Nat. Rev. Gastroenterol. Hepatol.* **15**(1), 11–20 (2018).
7. R. J. Wong, M. Aguilar, R. Cheung, R. B. Perumpail, S. A. Harrison, Z. M. Younossi, and A. Ahmed, "Nonalcoholic steatohepatitis is the second leading etiology of liver disease among adults awaiting liver transplantation in the United States," *Gastroenterology* **148**(3), 547–555 (2015).
8. R. J. Wong, R. Cheung, and A. Ahmed, "Nonalcoholic steatohepatitis is the most rapidly growing indication for liver transplantation in patients with hepatocellular carcinoma in the U.S.," *Hepatology* **59**(6), 2188–2195 (2014).
9. E. Fabbrini, S. Sullivan, and S. Klein, "Obesity and nonalcoholic fatty liver disease: Biochemical, metabolic, and clinical implications," *Hepatology* **51**(2), 679–689 (2010).
10. H. B. El-Serag, T. Tran, and J. E. Everhart, "Diabetes Increases the Risk of Chronic Liver Disease and Hepatocellular Carcinoma," *Gastroenterology* **126**(2), 460–468 (2004).
11. S. Kim, J. Cho, B. Ku, M. Jun, G. Kim, H. Yoo, S. Park, and J. U. Kim, "Variability of electrochemical skin conductance for screening diabetes mellitus," *Biomed. Eng. Lett.* **9**(2), 267–274 (2019).
12. A. Seppälä-Lindroos, S. Vehkavaara, A. M. Häkkinen, T. Goto, J. Westerbacka, A. Sovijärvi, J. Halavaara, and H. Yki-Järvinen, "Fat accumulation in the liver is associated with defects in insulin suppression of glucose production and serum free fatty acids independent of obesity in normal men," *J. Clin. Endocrinol. Metab.* **87**(7), 3023–3028 (2002).
13. H. Wobser, C. Dorn, T. S. Weiss, T. Amann, C. Bollheimer, R. Büttner, J. Schölmerich, and C. Hellerbrand, "Lipid accumulation in hepatocytes induces fibrogenic activation of hepatic stellate cells," *Cell Res.* **19**(8), 996–1005 (2009).
14. J. C. Cohen, J. D. Horton, and H. H. Hobbs, "Human Fatty Liver Disease: Old Questions and New Insights," *Science* **332**(6037), 1519–1523 (2011).

15. F. Marra, A. Gastaldelli, G. Svegliati Baroni, G. Tell, and C. Tiribelli, "Molecular basis and mechanisms of progression of non-alcoholic steatohepatitis," *Trends Mol. Med.* **14**(2), 72–81 (2008).
16. S. Schuster, D. Cabrera, M. Arrese, and A. E. Feldstein, "Triggering and resolution of inflammation in NASH," *Nat. Rev. Gastroenterol. Hepatol.* **15**(6), 349–364 (2018).
17. S. S. Rensen, Y. Slaats, J. Nijhuis, A. Jans, V. Bieghs, A. Driessen, E. Malle, J. W. Greve, and W. A. Buurman, "Increased Hepatic Myeloperoxidase Activity in Obese Subjects with Nonalcoholic Steatohepatitis," *Am. J. Pathol.* **175**(4), 1473–1482 (2009).
18. M. Kitade, H. Yoshiji, R. Noguchi, Y. Ikenaka, K. Kaji, Y. Shirai, M. Yamazaki, M. Uemura, J. Yamao, M. Fujimoto, A. Mitoro, M. Toyohara, M. Sawai, M. Yoshida, C. Morioka, T. Tsujimoto, H. Kawaratani, and H. Fukui, "Crosstalk between angiogenesis, cytokeratin-18, and insulin resistance in the progression of non-alcoholic steatohepatitis," *World J. Gastroenterol.* **15**(41), 5193–5199 (2009).
19. F. Kanwal, J. R. Kramer, S. Mapakshi, Y. Natarajan, M. Chayanupatkul, P. A. Richardson, L. Li, R. Desiderio, A. P. Thrift, S. M. Asch, J. Chu, and H. B. El-Serag, "Risk of Hepatocellular Cancer in Patients With Non-Alcoholic Fatty Liver Disease," *Gastroenterology* **155**(6), 1828–1837.e2 (2018).
20. K. Yasui, E. Hashimoto, Y. Komorizono, K. Koike, S. Arii, Y. Imai, T. Shima, Y. Kanbara, T. Saibara, T. Mori, S. Kawata, H. Uto, S. Takami, Y. Sumida, T. Takamura, M. Kawanaka, and T. Okanoue, "Characteristics of Patients With Nonalcoholic Steatohepatitis Who Develop Hepatocellular Carcinoma," *Clin. Gastroenterol. Hepatol.* **9**(5), 428–433 (2011).
21. A. J. Sanyal, "Past, present and future perspectives in nonalcoholic fatty liver disease," *Nat. Rev. Gastroenterol. Hepatol.* **16**(6), 377–386 (2019).
22. G. Musso, M. Cassader, and R. Gambino, "Non-alcoholic steatohepatitis: Emerging molecular targets and therapeutic strategies," *Nat. Rev. Drug Discovery* **15**(4), 249–274 (2016).
23. E. Kim, Y. Lee, S. Lee, and S. B. Park, "Discovery, Understanding, and Bioapplication of Organic Fluorophore: A Case Study with an Indolizine-Based Novel Fluorophore, Seoul-Fluor," *Acc. Chem. Res.* **48**(3), 538–547 (2015).
24. E. Kim, S. Lee, and S. B. Park, "A Seoul-Fluor-based bioprobe for lipid droplets and its application in image-based high throughput screening," *Chem. Commun.* **48**(17), 2331 (2012).
25. Y. Hwang, H. Yoon, K. Choe, J. Ahn, J. H. Jung, J.-H. Park, and P. Kim, "In vivo cellular-level real-time pharmacokinetic imaging of free-form and liposomal indocyanine green in liver," *Biomed. Opt. Express* **8**(10), 4706 (2017).
26. Y. Hwang, J. Ahn, J. Mun, S. Bae, Y. U. Jeong, N. A. Vinokurov, and P. Kim, "In vivo analysis of THz wave irradiation induced acute inflammatory response in skin by laser-scanning confocal microscopy," *Opt. Express* **22**(10), 11465 (2014).
27. K. Choe, J. Y. Jang, I. Park, Y. Kim, S. Ahn, D. Y. Park, Y. K. Hong, K. Alitalo, G. Y. Koh, and P. Kim, "Intravital imaging of intestinal lacteals unveils lipid drainage through contractility," *J. Clin. Invest.* **125**(11), 4042–4052 (2015).
28. H. Seo, Y. Hwang, K. Choe, and P. Kim, "In vivo quantitation of injected circulating tumor cells from great saphenous vein based on video-rate confocal microscopy," *Biomed. Opt. Express* **6**(6), 2158 (2015).
29. S. Ahn, K. Choe, S. Lee, K. Kim, E. Song, H. Seo, I. Kim, and P. Kim, "Intravital longitudinal wide-area imaging of dynamic bone marrow engraftment and multilineage differentiation through nuclear-cytoplasmic labeling," *PLoS One* **12**(11), e0187660 (2017).
30. I. Park, K. Choe, H. Seo, Y. Hwang, E. Song, J. Ahn, Y. Hwan Jo, and P. Kim, "Intravital imaging of a pulmonary endothelial surface layer in a murine sepsis model," *Biomed. Opt. Express* **9**(5), 2383–2393 (2018).
31. Q. M. Anstee and R. D. Goldin, "Mouse models in non-alcoholic fatty liver disease and steatohepatitis research," *Int. J. Exp. Pathol.* **87**(1), 1–16 (2006).
32. Y. Takahashi, Y. Soejima, and T. Fukusato, "Animal models of nonalcoholic fatty liver disease / nonalcoholic steatohepatitis," *World J. Gastroenterol.* **18**(19), 2300–2308 (2012).
33. S. Caldwell, Y. Ikura, D. Dias, K. Isomoto, A. Yabu, C. Moskaluk, P. Pramoonjago, W. Simmons, H. Scruggs, N. Rosenbaum, T. Wilkinson, P. Toms, C. K. Argo, A. M. S. Al-Osaimi, and J. A. Redick, "Hepatocellular ballooning in NASH," *J. Hepatol.* **53**(4), 719–723 (2010).
34. Y. Takahashi and T. Fukusato, "Histopathology of nonalcoholic fatty liver disease/nonalcoholic steatohepatitis," *World J. Gastroenterol.* **20**(42), 15539–15548 (2014).
35. Z. Hall, N. J. Bond, T. Ashmore, F. Sanders, Z. Ament, X. Wang, A. J. Murray, E. Bellafante, S. Virtue, A. Vidal-Puig, M. Allison, S. E. Davies, A. Koulman, M. Vacca, and J. L. Griffin, "Lipid zonation and phospholipid remodeling in nonalcoholic fatty liver disease," *Hepatology* **65**(4), 1165–1180 (2017).
36. T. Kietzmann, "Metabolic zonation of the liver: The oxygen gradient revisited," *Redox Biol.* **11**, 622–630 (2017).
37. S. Pieschl, E. Stahl, and R. Bromme, "Contribution of de novo fatty acid synthesis to hepatic steatosis and insulin resistance: lessons from genetically engineered mice," *J. Clin. Invest.* **118**(3), 389–400 (2003).
38. B. Vollmar and M. D. Menger, "The hepatic microcirculation: Mechanistic contributions and therapeutic targets in liver injury and repair," *Physiol. Rev.* **89**(4), 1269–1339 (2009).
39. J. K. C. Lau, X. Zhang, and J. Yu, "Animal models of non-alcoholic fatty liver disease: current perspectives and recent advances," *J. Pathol.* **241**(1), 36–44 (2017).
40. F. Caballero, A. Fernández, N. Matías, L. Martínez, R. Fucho, M. Elena, J. Caballeria, A. Morales, J. C. Fernández-Checa, and C. García-Ruiz, "Specific contribution of methionine and choline in nutritional nonalcoholic steatohepatitis: Impact on mitochondrial S-adenosyl-L-methionine and glutathione," *J. Biol. Chem.* **285**(24), 18528–18536 (2010).

41. W. Liu and J. Yao, "Photoacoustic microscopy: principles and biomedical applications," *Biomed. Eng. Lett.* **8**(2), 203–213 (2018).
42. W. Choi, E. Y. Park, S. Jeon, and C. Kim, "Clinical photoacoustic imaging platforms," *Biomed. Eng. Lett.* **8**(2), 139–155 (2018).
43. R. F. Mansour, "Deep-learning-based automatic computer-aided diagnosis system for diabetic retinopathy," *Biomed. Eng. Lett.* **8**(1), 41–57 (2018).
44. S. Ballestri, F. Nascimbeni, E. Baldelli, A. Marrazzo, D. Romagnoli, and A. Lonardo, "NAFLD as a Sexual Dimorphic Disease: Role of Gender and Reproductive Status in the Development and Progression of Nonalcoholic Fatty Liver Disease and Inherent Cardiovascular Risk," *Adv. Ther.* **34**(6), 1291–1326 (2017).
45. Z. M. Younossi, M. Stepanova, F. Negro, S. Hallaji, Y. Younossi, B. Lam, and M. Srishord, "Nonalcoholic fatty liver disease in lean individuals in the United States," *Medicine* **91**(6), 319–327 (2012).
46. M. Ganz, T. Csak, and G. Szabo, "High fat diet feeding results in gender specific steatohepatitis and inflammasome activation," *World J. Gastroenterol.* **20**(26), 8525–8534 (2014).
47. J. J. Pan and M. B. Fallon, "Gender and racial differences in nonalcoholic fatty liver disease," *World J. Hepatol.* **6**(5), 274–283 (2014).
48. R. Gebhardt and M. Matz-Soja, "Liver zonation: Novel aspects of its regulation and its impact on homeostasis," *World J. Gastroenterol.* **20**(26), 8491–8504 (2014).
49. L. Ritsma, E. J. A. Steller, E. Beerling, C. J. M. Loomans, A. Zomer, C. Gerlach, N. Vrisekoop, D. Seinstra, L. Van Gurp, R. Schäfer, D. A. Raats, A. De Graaff, T. N. Schumacher, E. J. P. D. Koning, I. H. B. Rinkes, O. Kranenburg, and J. Van Rheenen, "Intravital microscopy through an abdominal imaging window reveals a pre-micrometastasis stage during liver metastasis," *Sci. Transl. Med.* **4**(158), 158ra145 (2012).
50. L. Ritsma, E. J. A. Steller, S. I. J. Ellenbroek, O. Kranenburg, I. H. M. Borel Rinkes, and J. Van Rheenen, "Surgical implantation of an abdominal imaging window for intravital microscopy," *Nat. Protoc.* **8**(3), 583–594 (2013).
51. S. I. J. Ellenbroek and J. Van Rheenen, "Imaging hallmarks of cancer in living mice," *Nat. Rev. Cancer* **14**(6), 406–418 (2014).
52. I. Park, S. Hong, Y. Hwang, and P. Kim, "A novel pancreatic imaging window for stabilized longitudinal in vivo observation of pancreatic islets in murine model," *Diabetes Metab.* **44**(1), 193–198 (2020).